



Brojomohun College, Barisal

Subject Name

THESIS ON
Calcium Manganese Titanium Oxide (CaMnTiO_3)

Supervised By

Teacher Name

Lecturer

Faculty of Faculty Name

Brojomohun College, Barisal

Submitted By

Your Name

ID: XXXXXXXXXXXXXX

Publish Year **2016-2017**

26 October, 2016

Declaration

This is to certify that this project is our original work. No part of this has been submitted elsewhere partially or fully for the award of any other degree. Any material reproduced in this project has been properly acknowledged.

Name: Your Name
ID: XXXXXXXXXXXXX

Approval

The Thesis titled “Calcium Manganese Titanium Oxide” has been submitted to the following respected members of the Board of Examiners of Faculty Name in complete fulfillment of the requirements for the department of department name and engineering on Date by the following student and has been accepted satisfactory.

Teacher Name

Lecturer

Department of Department Name

College Name

Teacher Name

Head of the Department

Department Department Name

College Name

Teacher Name

Dean in Charge

Department of Department Name

College Name

Teacher Name

Vice Chancellor

Department of Department Name

College Name

Acknowledgements

We would like to take the chance to express our gratitude to our honorable teacher & Supervisor Teacher Name, for his continuous guidance and support regarding this report. Besides this, I have found so many sincere and productive advices from many people that we would like pay homage to them.

Table of Contents

Chapter 1: Surface composition and chemical states of calcium manganites **Error! Bookmark not defined.**

Abstract.....	6
1.1 Introduction	8
1.2 Sample preparation	8
1.3 Backscattering spectroscopy (BS) measurements	9
1.4 Determination of atomic composition.....	10
1.5 XPS and XRD measurements.....	11
1.6 Results and discussion	16
1.7 Summary	21

Chapter 2: Structure of Perovskite..... 22

2.1 Overview	23
2.2 Structure	23
2.3 Common occurrence	24
2.4 Material properties.....	24
2.5 Applications.....	25
2.6 Photovoltaics.....	25
2.7 Lasers	26
2.8 Light Emitting Diodes	26
2.9 Photoelectrolysis.....	27

Chapter 3: AN EXPERIMENTAL AND THEORETICAL INSIGHT OF CALCIUM TITANATE	22
2.1 Overview	23
2.2 Structure	23
2.3 Common occurrence	24
2.4 Material properties	24
2.5 Applications.....	25
2.6 Photovoltaics.....	25
2.7 Lasers	26
2.8 Light Emitting Diodes	26
REFERENCES	35

SURFACE COMPOSITION AND CHEMICAL STATES OF CALCIUM MANGANITES

ABSTRACT

This paper describes investigations on atomic composition and chemical states of sintered calcium manganites discs in surface and near surface regions. The atomic composition was determined by 3.05 MeV $^{16}\text{O}(\alpha,\alpha)^{16}\text{O}$ resonance elastic scattering while the chemical states by, X-ray photoelectron spectroscopy (XPS). The specimens examined included undoped and donor (Y^{3+} , Bi^{3+}) doped CaMnO_3 , and Ca-excess and Mn-excess manganites namely Ca_2MnO_4 and CaMn_2O_4 respectively. Calcium manganite powder used in the preparation of discs was synthesized by a wet chemical method. X-ray diffraction (XRD) results indicated that all the discs are monophasic except CaMn_2O_4 , which contained ~98% requisite manganite.

The atomic compositions of undoped specimens are close to the stoichiometric value while Y^{3+} and Bi^{3+} doped specimens are deficient in Mn and O respectively. The O deficiency may be responsible for comparatively higher electrical conductivity of Bi^{3+} doped specimen. Some of the specimens were also examined subsequent to their annealing in low PO_2 atmosphere.

This treatment produced significant compositional and structural modifications in the near surface regions. Mn(2p) electrons have identical binding energies in the sintered discs; therefore the valence states of Mn could not be discerned. However lesser binding energies of these electrons in annealed CaMnO_3 indicated the existence of Mn(II)/Mn(III) in the specimen.

1.1 INTRODUCTION

Manganites with perovskite structure exhibit several interesting electronic and magnetic phenomena such as insulator-metal transition and colossal magnetoresistance (CMR). Consequently, these materials have been intensively studied in recent years. These oxides can be represented by a general formula $\text{Ln}_{1-x}\text{AxMnO}_3$ with Ln being a rare earth element and A, an alkaline earth element.

The properties of materials depend on the content of x, nature and extent of doping and processing parameters. CaMnO_3 , the basic unit of these perovskites, is itself of great interest. It is an n-type semiconducting oxide and exhibits anti ferromagnetic ordering at $T_N < 130 \text{ K}$ as well. Incorporation of dopants introduces significant changes in the electrical properties of the material. It can also be electron doped by annealing in lower PO_2 atmosphere to produce oxygen deficient nonstoichiometric perovskite, $\text{CaMnO}_{3-\delta}$. The electrical and magnetic properties of $\text{CaMnO}_{3-\delta}$ are influenced by oxygen content as well as the valence states of manganese.

Surface characterization of manganites is important in fabricating multilayer thin film devices that make use of the CMR properties. In the present work we have studied the atomic composition, in the near surface regions, of sintered discs of undoped and donor (3 at% Bi^{3+} and Y^{3+}) doped CaMnO_3 as well as Ca-excess and Mn-excess manganites namely Ca_2MnO_4 and CaMn_2O_4 respectively by 3.05 MeV $^{16}\text{O}(\alpha,\alpha)^{16}\text{O}$ elastic resonance scattering.

Some of the specimens were also examined subsequent to their annealing in hydrogen atmosphere to study the compositional and structural variations accompanying the reduction process. This resonance scattering with significantly higher cross section is a well established backscattering spectrometry technique for depth profiling oxygen in the near surface regions non-destructively. It has been used in the analysis of several oxide matrices including Y–Ba–Cu–O superconductors.

However such a study on manganites is lacking as most analytical studies deal with the determination of oxygen by classical chemical methods. The estimated composition has been discussed in correlation with structural and phase analysis of the ceramics by XRD. In addition, we have also investigated the chemical states of manganese in these oxides by XPS.

1.2 SAMPLE PREPARATION

Polycrystalline samples of calcium manganite were synthesized by a wet chemical method involving a redox reaction between Mn(VII) and Mn(II) salts in nitric acid medium the details of which are reported in a previous publication. Briefly concentrated HNO_3 was added to aqueous solution of KMnO_4 to maintain the pH in 1–2 range and heated to boiling conditions.

The homogeneous solution of $\text{Ca}(\text{NO}_3)_2 \cdot 4\text{H}_2\text{O}$ and $\text{MnSO}_4 \cdot \text{H}_2\text{O}$, mixed in the desired ratio, was added to the boiling KMnO_4 solution to precipitate $\text{MnO}_2 \cdot x\text{H}_2\text{O}$. Due to its larger porosity and high surface area, the precipitated $\text{MnO}_2 \cdot x\text{H}_2\text{O}$ adsorbed other cations. The pH was raised to 7 by adding 2 M ammonium carbonate to complete the precipitation of the metal cations.

The precipitate was filtered and washed with deionised water for complete removal of anions such as Cl^- and SO_4^{2-} and subsequently oven dried at 373 K. The dry powder was decomposed at 850 K followed by calcination at 1373 K for 5 h. The powder of calcium manganite thus obtained was mixed with 0.1 wt.% polyvinyl alcohol, a binder, and then pressed into pellets (thickness, 2 mm; diameter, 10 mm) in a hydraulic press at 200 MPa and subsequently sintered in air at 1573K for 3h. Specimens doped with 3at% Bi^{3+} and Y^{3+} were prepared by intimately mixing the oxides of Y and Bi in the requisite proportions with calcium manganite powder and calcining at 1000 K for 3h.

The doped powder was then pelletised and sintered as described earlier. Some of the sintered specimens were annealed in $\text{N}_2 + \text{H}_2$ (1:1) atmosphere at 1373 K for 2 h to produce O deficient manganites.

1.3 BACKSCATTERING SPECTROSCOPY (BS) MEASUREMENTS

The BS measurements were carried out using 3MV Tandetron at National Centre for Compositional Characterisation of Materials (NCCCM), Hyderabad. The a particle beam ($\lambda = 1.5$ mm) of requisite energy impinged on the targets at normal incidence in a typical scattering chamber.

The vacuum in scattering chamber, pumped by a turbomolecular pump, was about $2 \cdot 10^{-6}$ Torr. An electron suppressor with -900 V was placed in front of the samples. The particles scattered at 170° were measured with a surface barrier detector and the data acquired on a PC based multichannel analyser.

1.4 DETERMINATION OF ATOMIC COMPOSITION

The $^{16}\text{O}(\alpha, \alpha)^{16}\text{O}$ resonant scattering occurs at the surface when the target is bombarded with 3.05 MeV α particles. It occurs from deeper layers of the target at higher incident energies. Therefore the depth profiling of O is accomplished by increasing the incident beam energy beyond 3.05 MeV in steps.

The relative atomic composition of CaMn_pO_q by this method can be estimated by using the formula: $q = R \times [\epsilon(\text{Ca}) + p\epsilon(\text{Mn})]/[\epsilon(\text{Si})/2 + 1 - R \times \epsilon(\text{O})]$ where ϵ is the stopping cross section of the elements in the brackets, R is the ratio of resonant O yields for CaMn_pO_q and a 3000 \AA SiO_2 film, used as a standard for oxygen. The quantity p was determined from the BS spectrum by taking the signals of Ca and Mn into consideration.

It is noted that their scattering cross sections are Rutherford in the beam energy region used in the experiments. The depth scale was established by the relation $(E\alpha - E_r)/S(E)$ where $E\alpha$ is the energy of the incident beam, E_r is the resonance energy and $S(E)$ is the stopping power at E_r . The stopping cross sections and powers were computed by SRIM 2000. The density of the discs required for computing $S(E)$ was estimated by geometrical methods.

1.5 XPS AND XRD MEASUREMENTS

The XPS measurements were performed with VG-Scientific ESCALAB Mk200X machine, using $\text{AlK}\alpha$ X-rays in a vacuum of 2×10^{-9} Torr. The energy scale of the spectrometer was calibrated with pure Ag and Cu samples. The binding energies were measured with a precision of ± 0.25 eV.

The XRD measurements for identifying crystalline phases in the ceramics were carried out by a Scintag (USA) diffractometer with $\text{CuK}\alpha$ radiation.

1.5 RESULTS AND DISCUSSION

The specimens are well sintered to more than 95% of theoretical density. XRD results indicate the sintered discs of CaMnO_3 , undoped as well as doped with 3at% Y^{3+} and Bi^{3+} , are monophasic with perovskite structure and orthorhombic symmetry of space group Pbma. The disc of Ca_2MnO_4 is also phase singular having K_2NiF_4 type structure while that of CaMn_2O_4 contains ~98% of the desired manganite, with marokite structure together with the minor phase of CaMnO_3 . The annealing of CaMnO_3 and CaMn_2O_4 in hydrogen atmosphere resulted in the formation of defect rock salt CaMnO_2 , and $\text{CaMnO}_{2.5}$ of brownmillerite type structure, respectively. The different phases present in sintered and annealed specimens along with their crystal symmetries are given in **Table 1**.

Table 1
Phases, crystal symmetries and resistivities of calcium manganites at 293 K

Composition	Phase contents	Crystal symmetry	Resistivity ($\Omega \text{ cm}$)
CaMnO_3	Perovskite	Orthorhombic	0.84
CaMnO_3 (3 at% Y^{3+})	Perovskite	Orthorhombic	0.12
CaMnO_3 (3 at% Bi^{3+})	Perovskite	Orthorhombic	0.06
Ca_2MnO_4	K_2NiF_4 type structure	Tetragonal	—
CaMn_2O_4	98.5% Marokite 1.5% Perovskite	Orthorhombic Cubic	8×10^3
CaMnO_3^a	Rock salt (CaMnO_2)	Cubic	—
$\text{CaMn}_2\text{O}_4^b$	Brownmillerite ($\text{CaMnO}_{2.5}$)	Cubic	—
$\text{CaMn}_2\text{O}_4^c$	88% Marokite 12% Perovskite	Orthorhombic Cubic	—

(—): Not measured.

^a CaMnO_3 annealed in $\text{N}_2 + \text{H}_2$ (1:1) atmosphere at 1373 K for 3 h.

^b CaMn_2O_4 annealed in $\text{N}_2 + \text{H}_2$ (1:1) atmosphere at 1373 K for 3 h (top portion).

^c CaMn_2O_4 annealed in $\text{N}_2 + \text{H}_2$ (1:1) atmosphere at 1373 K for 3 h (cleaved portion).

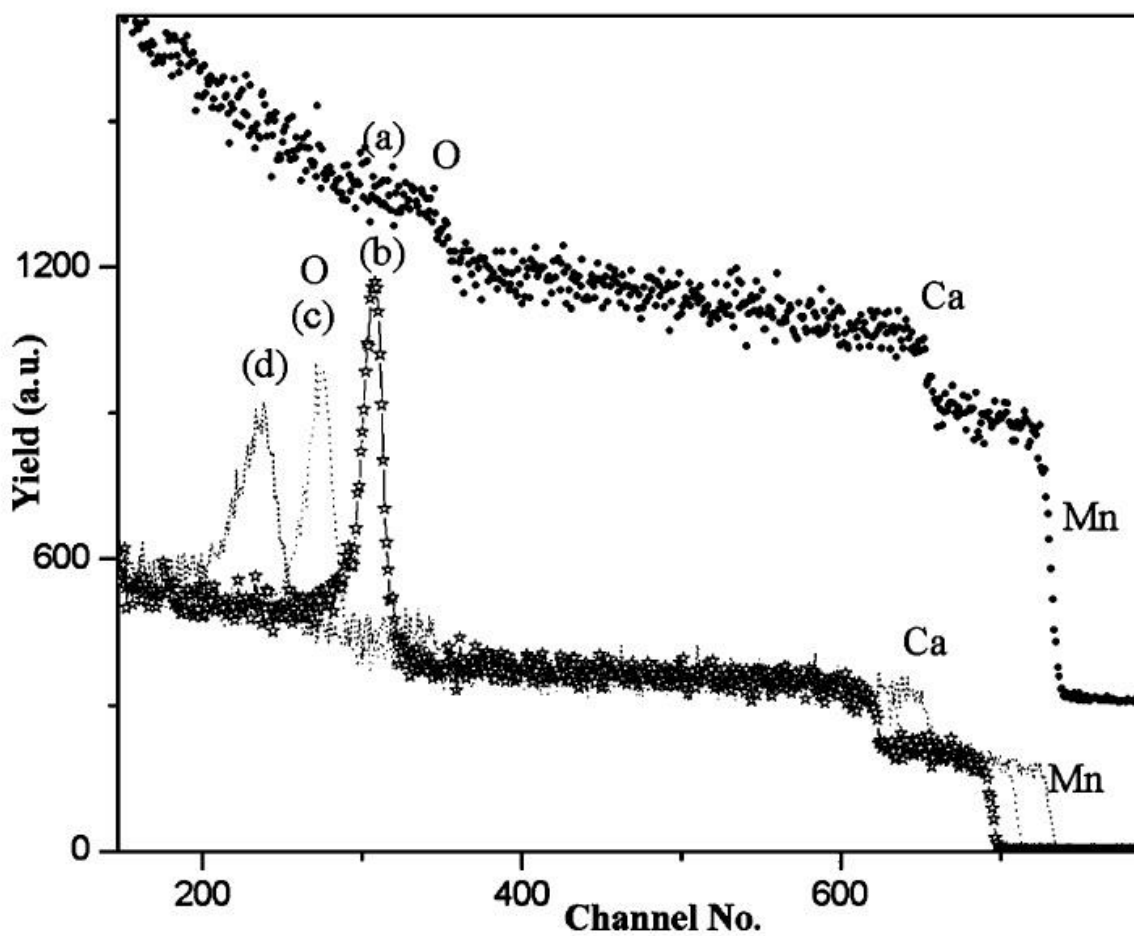


Figure 1.5.1: MeV α -RBS spectrum from CaMnO_3 and (b), (c) and (d) depth profile of oxygen in CaMnO_3 obtained with 3.07, 3.13 and 3.23 MeV α particles respectively.

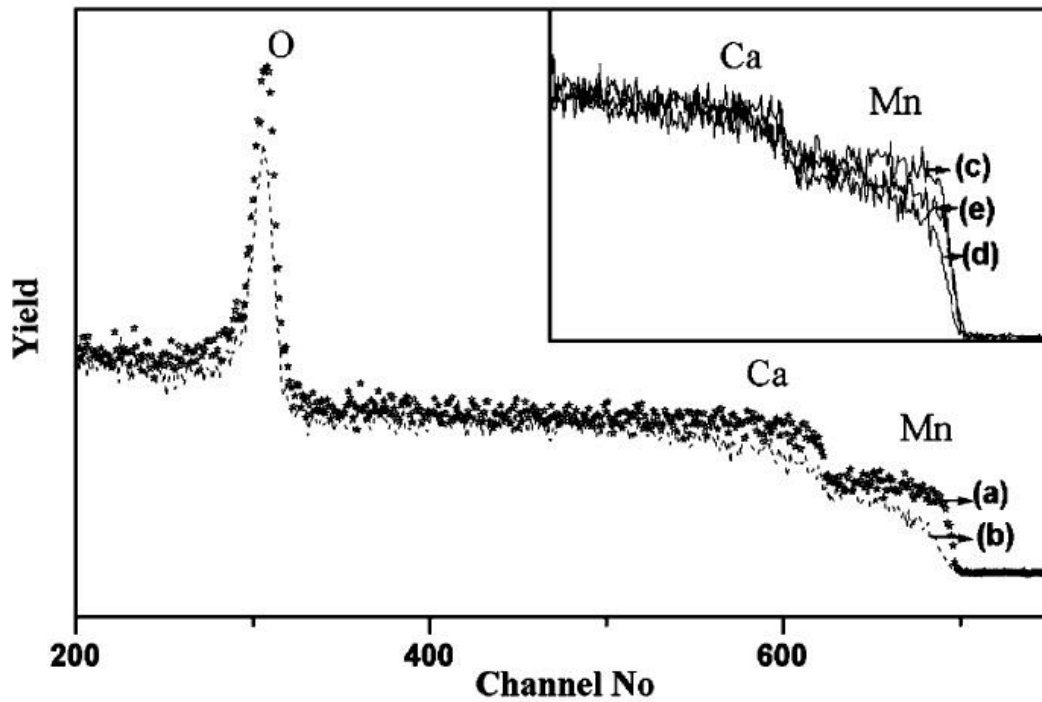


Figure 1.5.2: MeV α -backscattered spectra from (a) sintered CaMnO_3 and (b) after annealing it in hydrogen atmosphere. Inset shows the leading edges of Mn and Ca from (c) sintered CaMn_2O_4 (d) after annealing in hydrogen and (e) cracked interior surface of the annealed specimen.

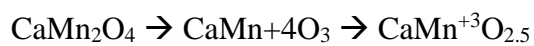
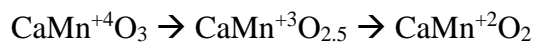
Figure 1.5.1(b)–(d) shows backscattered spectra from an undoped sintered CaMnO_3 specimen recorded with 3.07, 3.13 and 3.23 MeV α particles for depth profile measurements of oxygen. The occurrence of oxygen signal as a strong peak is due to $^{16}\text{O}(\alpha, \alpha)^{16}\text{O}$ resonant scattering. This approach is clearly advantageous over conventional RBS where the oxygen signal, as shown in Fig. 1.5.1(a), appears a weak step over the signals of Ca and Mn. The oxygen signal in Fig. 1(b)–

d) is a measure of its content at a depth of about 600 Å, 2500 Å and 5300 Å respectively. The height of oxygen signal decreases while its width increases with beam energy due to straggling effects but the area under the signal is constant for a homogeneous target.

Fig. 1.5.2(a) is the backscattered spectrum for an undoped sintered CaMnO_3 while Fig. 2(b) is from the same specimen annealed in hydrogen atmosphere. These spectra are normalized with respect to charge. It can be readily seen that in comparison to the sintered specimen, the annealed specimen has two significantly different spectral features: (1) the oxygen signal intensity is diminished and (2) the slopes of the leading edges of cations, Mn in particular, are less. These features are indicative of surface modifications resulting from annealing with the decrease in oxygen signal intensity signifying, expectedly, the reduction of the specimen. The second feature showing the depletion of Ca and Mn in the near surface regions is, however, interesting. The reduced specimen of CaMn_2O_4 also exhibits similar spectral features. The 3.07 MeV α backscattered spectra from this manganite and its annealed form are shown in Fig. 1.5.2(c) and (d) respectively for illustration. The specimen had in fact cracked horizontally into two parts during annealing. The spectrum in Fig. 1.5.2(d) is from the top part of the cracked sample. The underlying part was also examined along the surface exposed due to cracking and the resulting spectrum is shown in Fig. 1.5.2(e). It is observed by comparing the spectra in Fig. 1.5.2(c)-(e) that the slopes of the leading edges of Ca and Mn for the bottom part are more than those of the corresponding top part of annealed disc but still less than the sintered specimen. This can be attributed to the mild reduction of the specimen with crack facilitating the process. It is supported by the fact that the bottom part contains marokite as the major phase (88%) while the top part as mentioned earlier, contains only brownmillerite phase. It suggests that the interiors of the samples were not affected by annealing. The atomic composition of different specimens as a function of depth determined by 3.05 MeV $^{16}\text{O}(\alpha,\alpha)^{16}\text{O}$ resonant scattering is listed in Table 1. The errors in the estimation of atomic ratio of Ca to Mn and depth profiles of oxygen are about 3% and 6% respectively. These are however higher in the case of reduced specimens due to rapidly varying signal intensities. The estimated compositions of the undoped CaMnO_3 and Ca_2MnO_4 are in agreement with their respective nominal stoichiometries. The Y^{3+} doped CaMnO_3 specimen is deficient in Mn while the one doped with Bi^{3+} , in oxygen. It is to be noted that the oxygen content in the Bi^{3+} doped specimen is marginally less than the error associated with its measurement. Nevertheless in view of the

constancy of the value for repeated measurements, one at even higher depth, it can be surmised that the specimen is depleted in oxygen in comparison to undoped or Y^{3+} doped $CaMnO_3$. $CaMn_2O_4$ is enriched with Mn while oxygen stabilizes to its stoichiometric value at a depth of about 2000 Å. The excess of oxygen in surface regions may be due to adsorbed oxygen bearing species. In the case of annealed specimens, it is evident that reduction in hydrogen atmosphere causes considerable alteration in the composition with the relative contents of Mn and O decreasing significantly, particularly in the case of $CaMn_2O_4$. Further, the atomic composition of the bottom portion of the cracked specimen of $CaMn_2O_4$ is nearly identical to that of sintered $CaMn_2O_4$ due to its reduction to a lesser extent. It is in agreement with the conclusions drawn from the qualitative spectral analysis.

The reduction of $CaMnO_3$ and $CaMn_2O_4$ to $CaMnO_2$ and $CaMnO_{2.5}$ respectively involves loss of oxygen according to the following reactions:



The phase singularity of annealed $CaMnO_3$ is in agreement with the above formalism. However, the conformity observed between the compositional and phase analyses of sintered specimens is lacking, as there is a significant gradient in the concentration of oxygen in the surface regions. Furthermore, the depletion of Ca and Mn in identical concentrations maintains the relative atomic ratio of Ca and Mn close to unity. The surface depletion of Mn on reduction is distinctly observed in the case of $CaMn_2O_4$. So far as its reduction formalism is concerned, the formation of $CaMnO_3$ in the first step of the reaction is confirmed by increase in the content of $CaMnO_3$ phase from 1.5% in the sintered $CaMn_2O_4$ to 12% in the mildly reduced bottom portion of the cracked specimen. Calcium manganites thus formed are obviously accompanied by manganese oxides that are often non-stoichiometric. It is to be noted that depletion of Mn does not imply its loss, as manganese oxides are nonvolatile even at higher temperatures. Under this consideration, the present

observation can be ascribed to either precipitation and or migration of Mn bearing species during the reduction process, which escape detection, by XRD and BS. The non-stoichiometric phases formed often lack sufficiently large crystalline domains and therefore may not be identified by conventional structure determination technique.

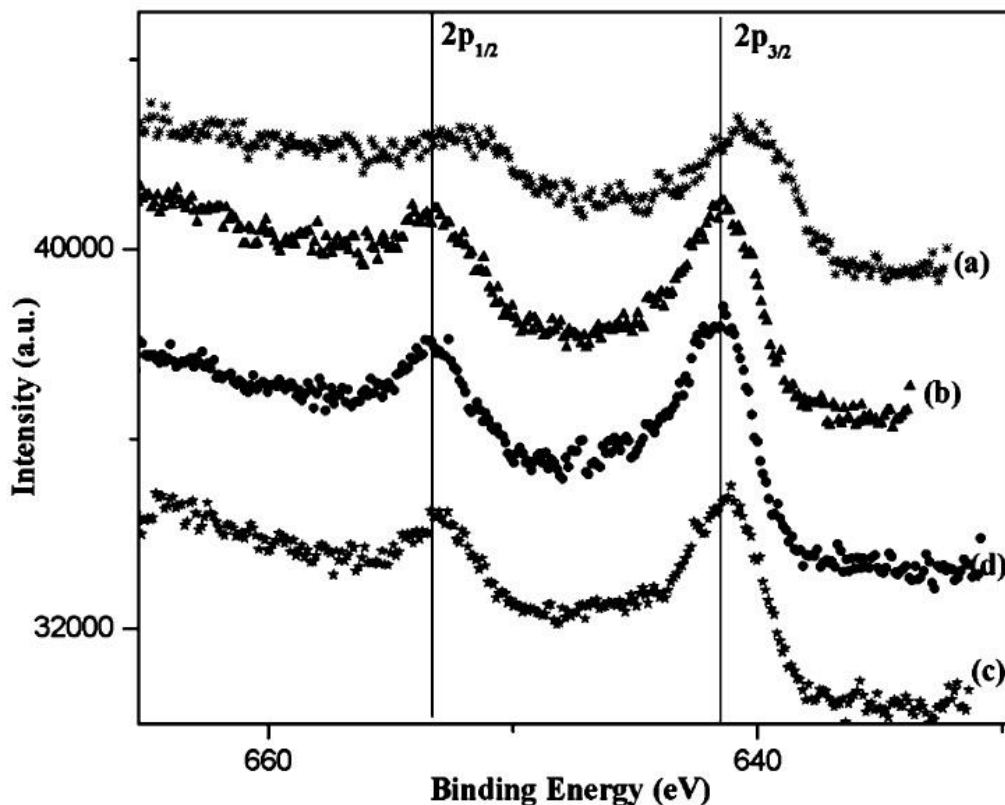


Figure 1.5.3: Mn(2p) electron spectra of (a) CaMnO_3 (reduced), (b) CaMn_2O_4 (sintered), (c) CaMn_2O_4 (reduced, top portion) and (d) CaMn_2O_4 (reduced, cracked portion).

The specimens were analysed by core level XPS to obtain information on the chemical states of the constituents. Fig. 1.5.3 shows the Mn(2p) electron spectra of different specimens. The spectra exhibit $2p_{1/2}$ and $2p_{3/2}$ spin-orbit doublets. The Mn(2p) peaks, in agreement with previous

studies, are broad and asymmetrical towards high binding energy side. Abbate et al. have explained the reasons for the larger breadth of the peaks.

Table 2
Atomic composition of calcium manganite specimens in near surface regions

Sample	Depth (Å)	Atomic composition ($N_{Ca}:N_{Mn}:N_O$)
CaMnO ₃	600	1.0:1.0:3.1
	2500	1.0:1.0:3.1
CaMnO ₃ ^a	600	1.0:0.9:1.5
	1700	1.0:0.9:2.2
	2500	1.0:0.8:2.4
CaMnO ₃ (3 at% Y ³⁺ doped)	600	1.0:0.9:3.2
	2500	1.0:0.9:3.1
CaMnO ₃ (3 at% Bi ³⁺ doped)	600	1.0:1.0:2.8
	2500	1.0:1.0:2.8
	5100	1.0:1.0:2.8
CaMn ₂ O ₄	800	1.0:2.2:4.4
	2800	1.0:2.2:4.1
	3800	1.0:2.2:4.2
CaMn ₂ O ₄ ^b	800	1.0:1.2:2.0
	2800	1.0:1.2:1.9
	3800	1.0:1.1:1.6
CaMn ₂ O ₄ ^c	800	1.0:2.0:3.8
	1900	1.0:2.1:3.9
	3800	1.0:2.0:4.1

^a CaMnO₃ annealed in N₂ + H₂ (1:1) atmosphere at 1373 K for 3 h.

^b CaMn₂O₄ annealed in N₂ + H₂ (1:1) atmosphere at 1373 K for 3 h (top portion).

^c CaMn₂O₄ annealed in N₂ + H₂ (1:1) atmosphere at 1373 K for 3 h (cracked bottom portion).

Oku et al. have measured the binding energies of Mn(2p_{3/2}) electrons in different manganese oxides. These are also listed in Table 2. It can be seen that the chemical shift is appreciable only in MnO and MnO₂. The study also concluded neither the two oxidation states of Mn in Mn₃O₄

nor Mn site differences in Mn_2O_3 are distinguishable by XPS. In previous XPS studies on CaMnO_3 and several $\text{CaMnO}_{3-\delta}$ compounds with different δ values, the binding energy of Mn $2p_{3/2}$ electrons was reported to be identical (641.9 eV) in each compound. However in the present studies, it is about 641.7 eV in all the specimens except annealed CaMnO_3 where it is about 640.6 eV. It is to be noted that the surfaces of reduced specimens were distinctly green providing indication of existence of Mn in +3 valence states. The higher binding energy of Mn $2p_{3/2}$ electrons in air sintered CaMnO_3 suggests Mn to be in +4 valence state, occupying sites with octahedral O coordination.

The reduction of CaMnO_3 involves introduction of O vacancies and conversion of Mn^{4+} ions into lower oxidation states. The lower binding energy in $\text{CaMnO}_{3-\delta}$ is indicative of this process. The differences in the binding energies in $\text{CaMnO}_{3-\delta}$ in the present study and may be due to different conditions of reduction. MnO and CaO also have rocksalt structure. The lower binding energies of Mn (2p) electrons in such samples eliminate the possibility of formation of MnO , which due to its pyrophoric nature, gets converted to Mn_3O_4 . Similarly CaO reacts with atmospheric CO_2 , to produce CaCO_3 . The C (1s) electron spectra of each specimen showed only one peak corresponding to the adventitious carbon. The absence of a peak in 287–289 eV in the C (1s) spectra, characteristic of CO_3^{2-} , is therefore indicative of the absence of CaO as well.

The binding energies of Ca(2p) electrons in the specimens are also nearly identical. The slight variation in their values is due to different crystal structures of the specimens (Table 3).

Table 3

Binding energies (eV) of Mn 2p and Ca 2p electrons in calcium manganites

Sample	Mn		Ca	
	2p _{3/2}	2p _{1/2}	2p _{3/2}	2p _{1/2}
CaMnO ₃	641.9	653.5	347.5	351.1
CaMnO ₃ ^a	640.8	652.2	347.3	351.0
CaMn ₂ O ₄	641.8	653.4	347.5	351.0
CaMn ₂ O ₄ ^b	641.4	653.0	347.3	351.0
CaMn ₂ O ₄ ^c	641.7	653.3	347.4	351.1
MnO	640.6	652.2	—	—
Mn ₃ O ₄	641.4	653.0	—	—
Mn ₂ O ₃	641.9	653.5	—	—
MnO ₂	642.2	653.8	—	—

^a CaMnO₃ annealed in N₂ + H₂ (1:1) atmosphere at 1373 K for 3 h.

^b CaMn₂O₄ annealed in N₂ + H₂ (1:1) atmosphere at 1373 K for 3 h (top portion).

^c CaMn₂O₄ annealed in N₂ + H₂ (1:1) atmosphere at 1373 K for 3 h (cracked bottom portion).

Fig. 1.5.4 shows the temperature dependence of electrical resistivity, ρ versus T , for undoped and doped CaMnO₃. It is evident that doping with either Y³⁺ or Bi³⁺ causes a decrease in the resistivity of CaMnO₃. The doped specimens exhibit metal to insulator transition at around 160 K.

The resistivity of manganites depends on several factors including the valence states of Mn and oxygen

non-stoichiometry. Double exchange mechanism which involves hopping of electrons from Mn^{3+} ($t^3_{2g}e_g$) onto Mn^{4+} (t^3_{2g}) is usually invoked to explain variations in resistivity. The doping of $CaMnO_3$ at Ca sites with trivalent Y^{3+} or Bi^{3+} ions introduces electrons by way of charge compensation leading to the formation Mn^{3+} in the matrix such that it is represented as

$Ca_{1-x}Y(Bi)_xMn^{4+}_{1-x}Mn^{3+}_xO_3$. Therefore the resistivities of the doped materials are less. Further, it is observed that the resistivity of Bi^{3+} doped specimen is the lowest, which can be attributed to its oxygen deficiency.

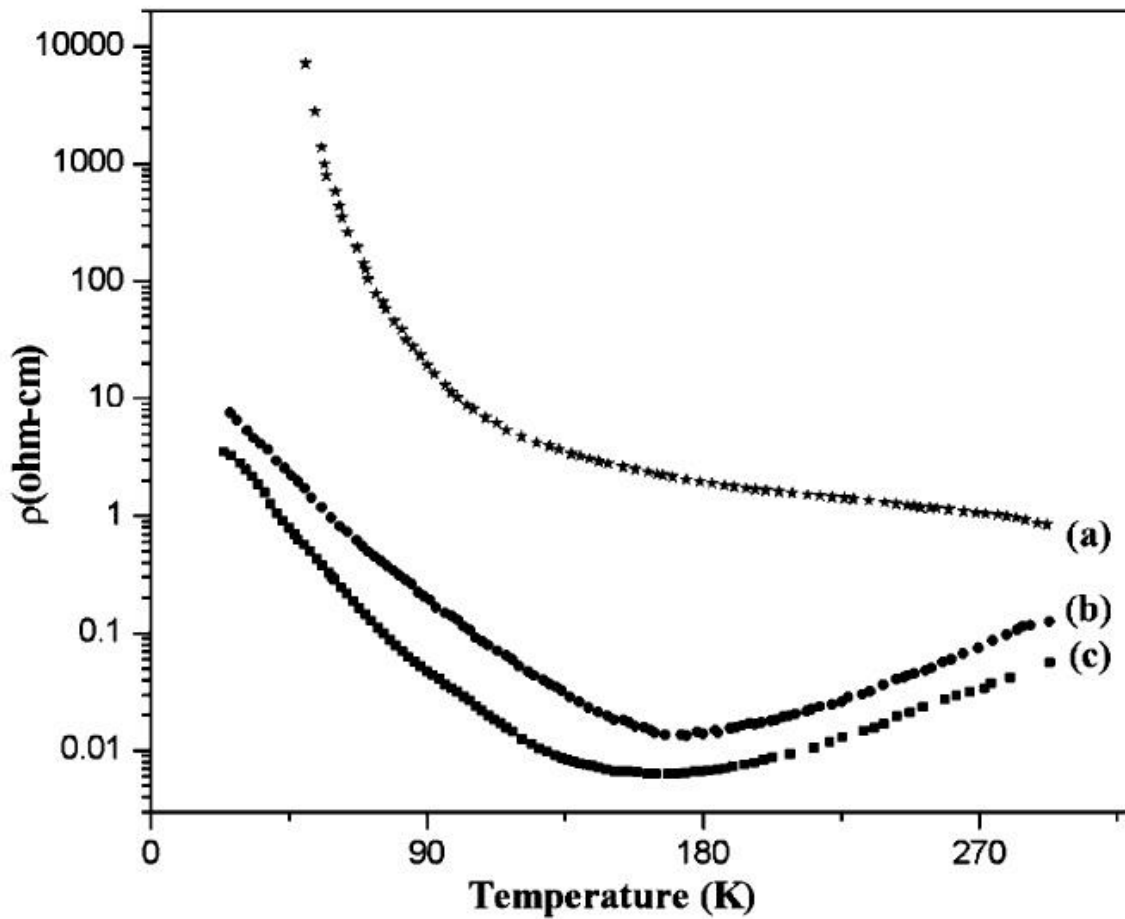


Figure 1.5.4: Resistivity versus temperature plot for (a) undoped, 3at% Y^{3+} and (c) 3at% Bi^{3+} doped $CaMnO_3$.

The removal of one oxygen ion (O^{2-}) results in the generation of two Mn^{3+} ions causing an increase in Mn(III) concentration and hence the increased conductivity of the material. However we could not explain the effect of Mn deficiency in the Y^{3+} doped specimen. The present study shows that dopants of similar charges may not introduce identical compositional changes. Resistivity measurements could not be performed on reduced specimens in view of the presence of micro cracks. However previous reports suggest that the resistivity of reduced manganites, $CaMnO_{3-\delta}$ is strongly influenced by oxygen deficiency, which controls the concentration of Mn^{3+} ions and, in turn the resistivity.

1.6 SUMMARY

3.05 MeV $^{16}O(\alpha,\alpha)^{16}O$ resonant scattering with enhanced sensitivity for oxygen provides the compositional analysis of calcium manganites with reasonably good accuracy. Doping in the Mn site of $CaMnO_3$ with donors such as Y^{3+} or Bi^{3+} causes compositional changes in the material, which affect its electrical characteristics. However the phase identity of $CaMnO_3$ (perovskite) is maintained on doping. Annealing of manganites in hydrogen atmosphere introduces significant structural and compositional changes that modify the BS spectral features of the parent manganites. XPS measurements suggest the existence of Mn(II)/Mn(III) in the annealed specimens.

STRUCTURE OF PEROVSKITE

A perovskite is any material with the same type of crystal structure as calcium titanium oxide (CaTiO_3), known as the perovskite structure, or $^{\text{XII}}\text{A}^{2+}\text{B}^{4+}\text{X}^{2-}_3$ with the oxygen in the face centers.

2.1 OVERVIEW

Perovskites take their name from the mineral, which was first discovered in the Ural mountains of Russia by Gustav Rose in 1839 and is named after Russian mineralogist L. A. Perovski (1792–1856). The general chemical formula for perovskite compounds is ABX_3 , where 'A' and 'B' are two cations of very different sizes, and X is an anion that bonds to both. The 'A' atoms are larger than the 'B' atoms.

The ideal cubic-symmetry structure has the B cation in 6-fold coordination, surrounded by an octahedron of anions, and the A cation in 12-fold cuboctahedral coordination. The relative ion size requirements for stability of the cubic structure are quite stringent, so slight buckling and distortion can produce several lower-symmetry distorted versions, in which the coordination numbers of A cations, B cations or both are reduced.

Natural compounds with this structure are perovskite, loparite, and the silicate perovskite bridgmanite.

2.2 STRUCTURE

The perovskite structure is adopted by many oxides that have the chemical formula ABO_3 . In the idealized cubic unit cell of such a compound, type 'A' atom sits at cube corner positions (0, 0, 0), type 'B' atom sits at body centre position (1/2, 1/2, 1/2) and oxygen atoms sit at face centred positions (1/2, 1/2, 0). (The diagram shows edges for an equivalent unit cell with A in body centre, B at the corners, and O in mid-edge).

The relative ion size requirements for stability of the cubic structure are quite stringent, so slight buckling and distortion can produce several lower-symmetry distorted versions, in which the coordination numbers of A cations, B cations or both are reduced.

Tilting of the BO_6 octahedra reduces the coordination of an undersized A cation from 12 to as low as 8. Conversely, off-centering of an undersized B cation within its octahedron allows it to attain a stable bonding pattern. The resulting electric dipole is responsible for the property of ferroelectricity and shown by perovskites such as $BaTiO_3$ that distort in this fashion.

The orthorhombic and tetragonal phases are most common non-cubic variants. Complex perovskite structures contain two different B-site cations. This results in the possibility of ordered and disordered variants.

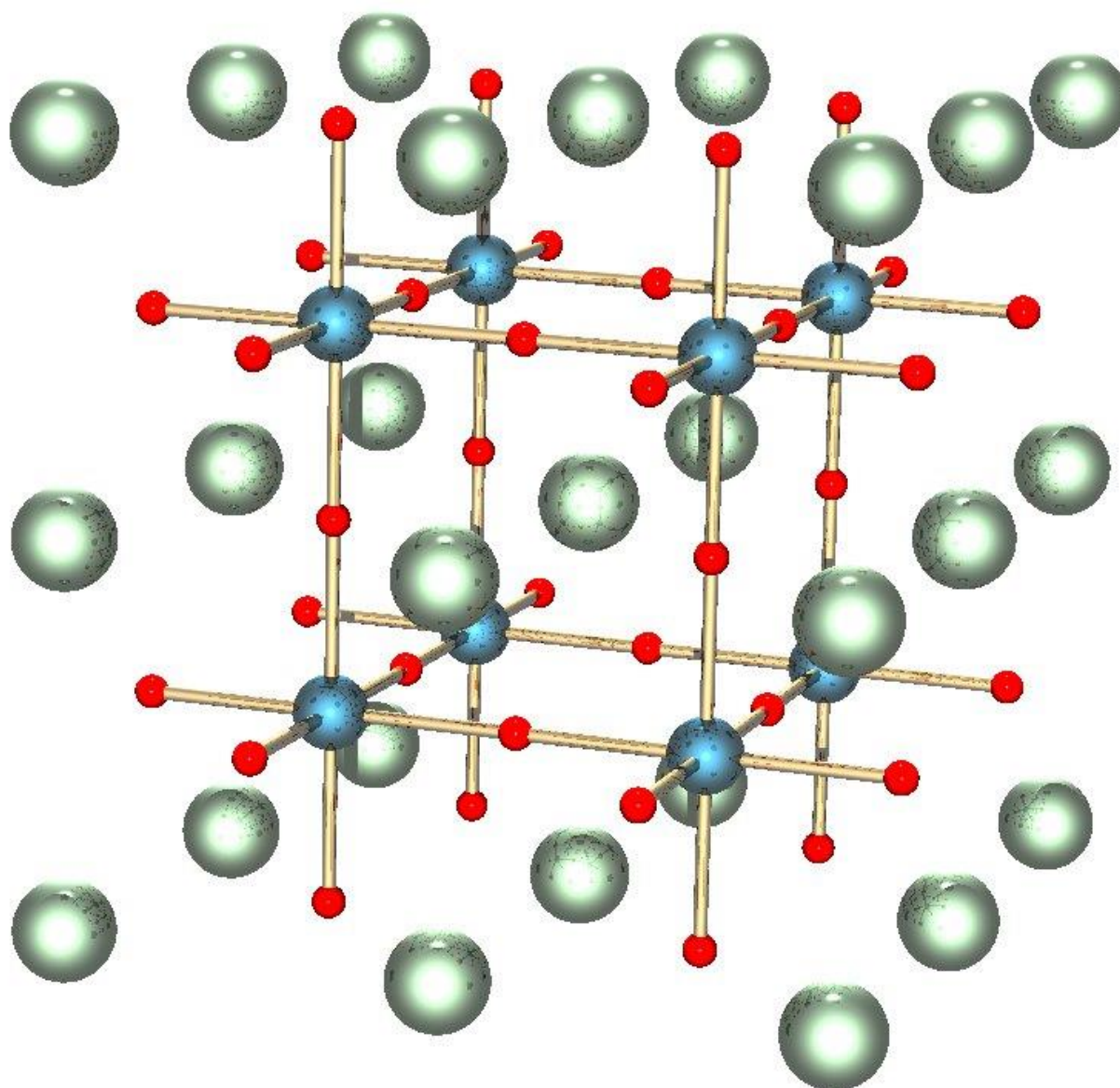


Figure 2.2.1: Structure of a perovskite with a chemical formula ABX_3 . The red spheres are X atoms (usually oxygens), the blue spheres are B-atoms (a smaller metal cation, such as Ti^{4+}), and the green spheres are the A-atoms (a larger metal cation, such as Ca^{2+}). Pictured is the undistorted cubic structure; the symmetry is lowered to orthorhombic, tetragonal or trigonal in many perovskites.

2.3 COMMON OCCURRENCE

The most common mineral in the Earth is bridgmanite, a magnesium-rich silicate which adopts the perovskite structure at high pressure. As pressure increases, the SiO_4^{4-} tetrahedral units in the dominant silica-bearing minerals become unstable compared with SiO_6^{8-} octahedral units.

At the pressure and temperature conditions of the lower mantle, the most abundant material is a perovskite-structured mineral with the formula $(\text{Mg,Fe})\text{SiO}_3$, with the second most abundant material likely the rocksalt-structured $(\text{Mg,Fe})\text{O}$ oxide, periclase.

At the high pressure conditions of the Earth's lower mantle, the pyroxene enstatite, MgSiO_3 , transforms into a denser perovskite-structured polymorph; this phase may be the most common mineral in the Earth. This phase has the orthorhombically distorted perovskite structure (GdFeO_3 -type structure) that is stable at pressures from ~ 24 GPa to ~ 110 GPa.

However, it cannot be transported from depths of several hundred km to the Earth's surface without transforming back into less dense materials. At higher pressures, MgSiO_3 perovskite transforms to post-perovskite.

Although the most common perovskite compounds contain oxygen, there are a few perovskite compounds that form without oxygen. Fluoride perovskites such as NaMgF_3 are well known. A large family of metallic perovskite compounds can be represented by RT_3M (R: rare-earth or other relatively large ion, T: transition metal ion and M: light metalloids).

The metalloids occupy the octahedrally coordinated "B" sites in these compounds. RPd_3B , RRh_3B and CeRu_3C are examples. MgCNi_3 is a metallic perovskite compound and has received lot of attention because of its superconducting properties. An even more exotic type of perovskite is represented by the mixed oxide-aurides of Cs and Rb, such as Cs_3AuO , which contain large alkali cations in the traditional "anion" sites, bonded to O^{2-} and Au^- anions.

2.4 MATERIAL PROPERTIES

Perovskite materials exhibit many interesting and intriguing properties from both the theoretical and the application point of view. Colossal magnetoresistance, ferroelectricity, superconductivity, charge ordering, spin dependent transport, high thermopower and the interplay of structural, magnetic and transport properties are commonly observed features in this family.

These compounds are used as sensors and catalyst electrodes in certain types of fuel cells and are candidates for memory devices and spintronics applications.



Figure 2.4.1: A Perovskite mineral (calcium titanate) from Kusa, Russia. Taken at the Harvard Museum of Natural History.

Many superconducting ceramic materials (the high temperature superconductors) have perovskite-like structures, often with 3 or more metals including copper, and some oxygen positions left vacant. One prime example is yttrium barium copper oxide which can be insulating or superconducting depending on the oxygen content.

Chemical engineers are considering a cobalt-based perovskite material as a replacement for platinum in catalytic converters in diesel vehicles.

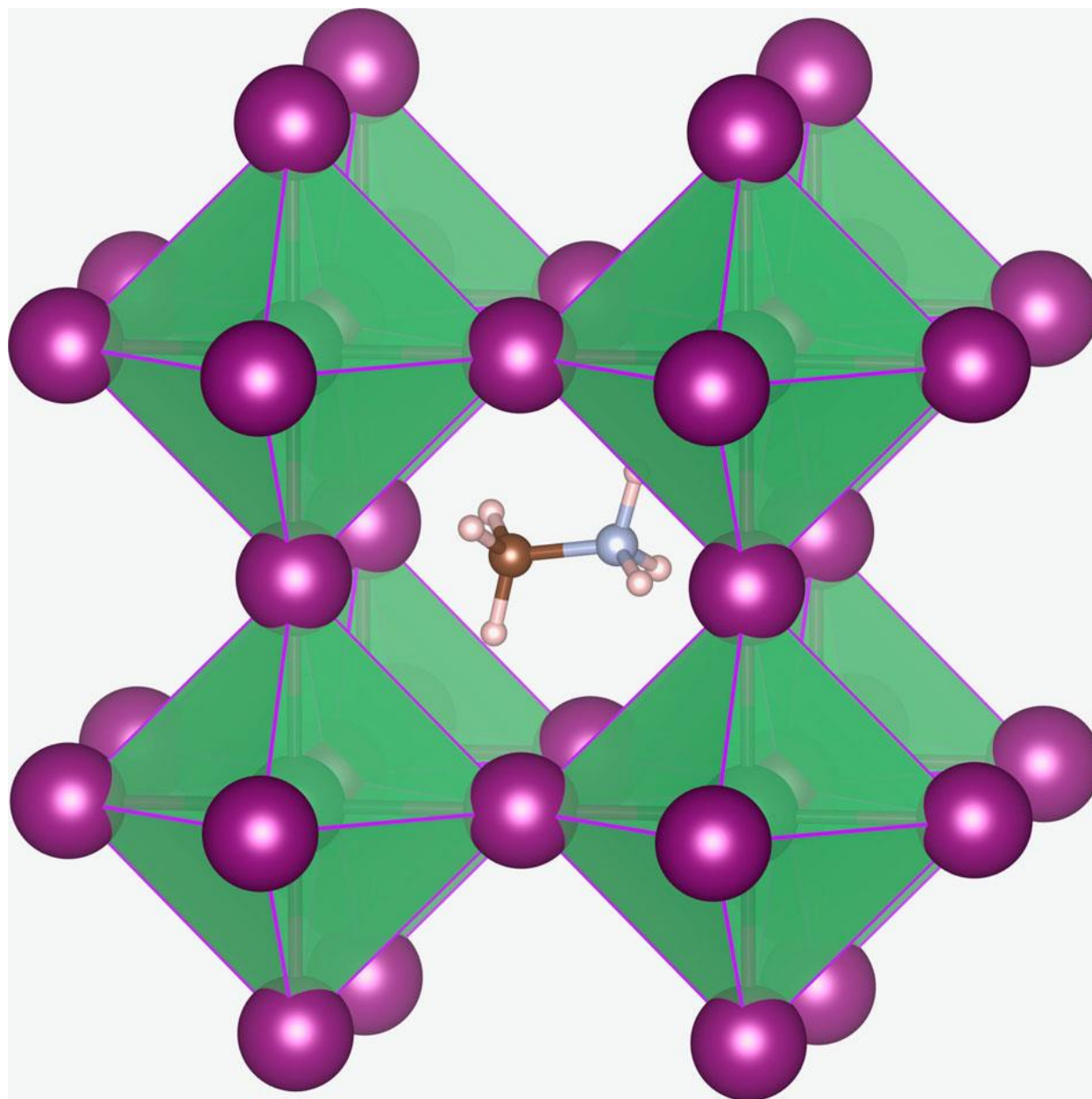


Figure 2.4.2: Crystal structure of $\text{CH}_3\text{NH}_3\text{PbX}_3$ perovskites ($\text{X}=\text{I}$, Br and/or Cl). The methylammonium cation (CH_3NH_3^+) is surrounded by PbX_6 octahedra.

2.5 APPLICATIONS

Physical properties of interest to materials science among perovskites include superconductivity, magnetoresistance, ionic conductivity, and a multitude of dielectric properties, which are of great importance in microelectronics and telecommunication.

Because of the flexibility of bond angles inherent in the perovskite structure there are many different types of distortions which can occur from the ideal structure. These include tilting of the octahedra, displacements of the cations out of the centers of their coordination polyhedra, and distortions of the octahedra driven by electronic factors (Jahn-Teller distortions).

2.6 PHOTOVOLTAICS

Synthetic perovskites have been identified as possible inexpensive base materials for high-efficiency commercial photovoltaics – they showed a conversion efficiency of up to 15% and can be manufactured using the same thin-film manufacturing techniques as that used for thin film silicon solar cells.

Methylammonium tin halides and methylammonium lead halides are of interest for use in dye-sensitized solar cells. In 2016, power conversion efficiency have reached 21%. [citation needed] In July 2016, a team of researchers led by Dr. Alexander Weber-Bargioni demonstrated that perovskite PV cells could reach a theoretical peak efficiency of 31%.

Among the methylammonium halides studied so far the most common is the methylammonium lead triiodide ($\text{CH}_3\text{NH}_3\text{PbI}_3$). It has a high charge carrier mobility and charge carrier lifetime that allow light-generated electrons and holes to move far enough to be extracted as current, instead of losing their energy as heat within the cell. $\text{CH}_3\text{NH}_3\text{PbI}_3$ effective diffusion lengths are some 100 nm for both electrons and holes.

Methylammonium halides are deposited by low-temperature solution methods (typically spin-coating). Other low-temperature (below 100 °C) solution-processed films tend to have

considerably smaller diffusion lengths. Stranks et al. described nanostructured cells using a mixed methylammonium lead halide ($\text{CH}_3\text{NH}_3\text{PbI}_{3-x}\text{Cl}_x$) and demonstrated one amorphous thin-film solar cell with an 11.4% conversion efficiency, and another that reached 15.4% using vacuum evaporation.

The film thickness of about 500 to 600 nm implies that the electron and hole diffusion lengths were at least of this order. They measured values of the diffusion length exceeding 1 μm for the mixed perovskite, an order of magnitude greater than the 100 nm for the pure iodide. They also showed that carrier lifetimes in the mixed perovskite are longer than in the pure iodide.

For $\text{CH}_3\text{NH}_3\text{PbI}_3$, open-circuit voltage (VOC) typically approaches 1 V, while for $\text{CH}_3\text{NH}_3\text{PbI}(\text{I},\text{Cl})_3$ with low Cl content, $\text{VOC} > 1.1$ V has been reported. Because the band gaps (E_g) of both are 1.55 eV, VOC-to- E_g ratios are higher than usually observed for similar third-generation cells. With wider bandgap perovskites, VOC up to 1.3 V has been demonstrated.

The technique offers the potential of low cost because of the low temperature solution methods and the absence of rare elements. Cell durability is currently insufficient for commercial use.

Planar heterojunction perovskite solar cells can be manufactured in simplified device architectures (without complex nanostructures) using only vapor deposition. This technique produces 15% solar-to-electrical power conversion as measured under simulated full sunlight.

2.7 LIGHT EMITTING DIODES

Also in 2008 researchers demonstrated that perovskite can generate laser light. LaAlO_3 doped with neodymium gave laser emission at 1080 nm. In 2014 it was shown that mixed methylammonium lead halide ($\text{CH}_3\text{NH}_3\text{PbI}_{3-x}\text{Cl}_x$) cells fashioned into optically pumped vertical-cavity surface-emitting lasers (VCSELs) convert visible pump light to near-IR laser light with a 70% efficiency.

2.8 LASERS

Due to their high photoluminescence quantum efficiencies, perovskites may be good candidates for use in light-emitting diodes (LEDs). However, the propensity for radiative recombination has mostly been observed at liquid nitrogen temperatures.

2.9 PHOTOELECTROLYSIS

In September 2014, researchers of EPFL in Lausanne, Switzerland reported achieving water electrolysis at 12.3% efficiency in a highly efficient and low-cost water-splitting cell using perovskite photovoltaics.

2.10 Synthesis

CaTiO_3 can be prepared by the combination of CaO and TiO_2 at temperatures $>1300^\circ\text{C}$. Sol-gel processes has been used to make a more pure substance, as well as lowering the synthesis temperature. These compounds synthesized are more compressible due to the powders from the sol-gel process as well and bring it closer to its calculated density ($\sim 4.04\text{ g/ml}$).

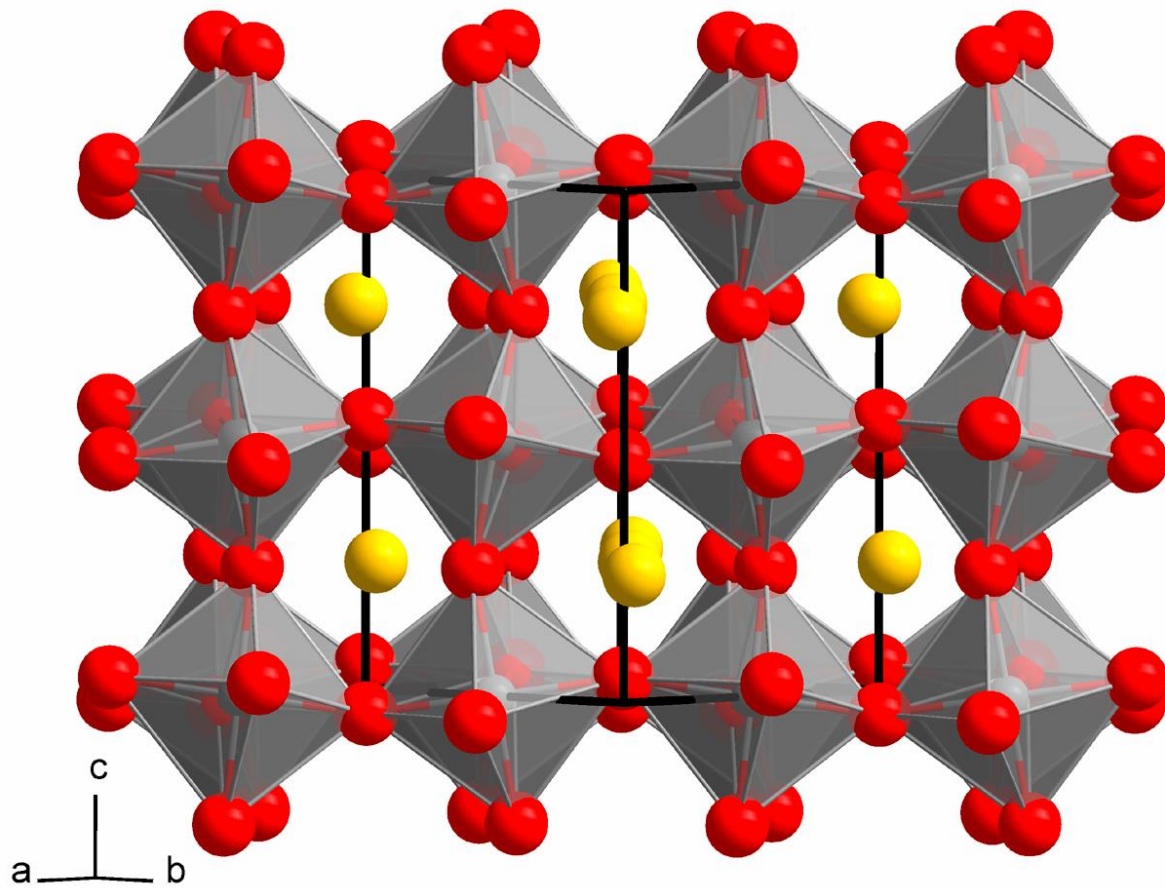


Figure 2.10.1: Crystal structure of the mineral perovskite (calcium titanate, CaTiO_3 ; orthorhombic, space group Pbmn). The perovskite structure type usually refers to the cubic structure (space group $\text{Pm}\bar{3}\text{m}$) found e.g. for strontium and barium-titanate. Due to the smaller size of the Ca^{2+} cations, the crystal structure of the CaTiO_3 prototype is slightly distorted and thus the cubic symmetry is reduced to orthorhombic. Crystallographic data:

AN EXPERIMENTAL AND THEORETICAL INSIGHT OF CALCIUM TITANATE

3.1 ABSTRACT

CaTiO₃ powders were synthesized using both a polymeric precursor method (CT_{ref}) and a microwave-assisted hydrothermal (CT_{HTMW}) method in order to compare the chemical and physical properties of the perovskite-based material as a function of the synthesis method. To this end, X-ray diffraction, Raman spectroscopy, inductively coupled plasma atomic emission spectroscopy and experimental Ti and Ca K-edge X-ray absorption near-edge structure spectroscopy, as well as measurements of photoluminescence (PL) emission, were used to characterize the typical bottom-up process of the CaTiO₃ perovskite phase at different times. Detailed Rietveld refinements show a random polycrystalline distortion in the powder structure, which can be associated with the tilting (α angle $< \text{O-Ti-O}$) between adjacent TiO₆ octahedra (intermediate range) for CT_{HTMW} samples and an intrinsic TiO₆ distortion (short range) in relation to the polymeric precursor CT_{ref} sample. These properties were further investigated by first-principles calculations based on the density functional theory at the B3LYP level. The relationship between this tilting on the PL profile is highlighted and discussed. Thus, a structural model derived from both experimental results and theoretical simulations reveals a close relationship between this tilting and the presence of intermediate energy states within the band gap which are mainly responsible for PL emissions.

3.2 PROPERTIES OF CALCIUM TITANATE

Order–disorder effects are the keys to many unsolved structural problems and unexplained structure-related properties in solid materials. In particular, structural order–disorder is always present in real materials and may play an important role in technological applications by altering their electronic and optical properties.

Therefore, physical principles that govern the structural state of a given perovskite and how that state may change have long been the subject of investigation and debate. Compounds with the perovskite structure, ABO_3 , and its derivatives are perhaps the most widely investigated owing to their significance to both fundamental research and the high potential for technological applications because of their diverse physical properties. Their electronic structures and photophysical properties have been the goal of much research; in particular, several efforts have been devoted to studying the photoluminescence (PL) emission of titanates such as $ATiO_3$ ($A = \text{Ca, Sr, Ba, Pb}$).

The PL emission in perovskite materials is considered to be closely related to the crystal structure and their corresponding distorted metal–oxygen polyhedra. In particular, TiO_6 octahedra in this family exhibit marked structural flexibility. Perhaps the most striking manifestation of such flexibility is the fact that under ambient conditions many titanates present structures with lower symmetries that can indeed be derived from the cubic aristotype structure ($Pm\bar{3}m$ space group) through the rotation or tilting of regular, rigid octahedra or due to the presence of distorted TiO_6 octahedra. It is significant that although the structure is distorted, the rotation/tilting does not disrupt the corner-sharing connectivity.

The tilting of the octahedral framework also plays a major role in determining the properties of oxide perovskites. Cooperative rotations can give rise to as many as Glazer tilt systems. In the seminal studies of Glazer and, more recently, those of both Woodward, and Howard and Stokes, the changes in symmetry resulting from different types of octahedral tilting have been systematized and rationalized. Glazer's notation specifies the magnitude and phase of the rotation of the octahedra about the three orthogonal axes of the aristotype cubic unit cell. For example, in the $CaTiO_3$ (CT) the notation is $a^-b^+a^-$, which implies unequal tilts about the x, y, and z axes. The

positive superscript indicates neighboring octahedra tilt in the same direction (in phase) while a negative superscript indicates the octahedra tilt in opposite directions (out of phase).

Although the precise mechanisms of these transformations remain elusive, both experimental and theoretical studies have shed light on these interesting phenomena. The present work focuses on links between the structure and the photoluminescent behavior of titanates with the parent mineral CaTiO_3 (CT) selected as a case study. In the framework of a more extended project aimed at the design and synthesis of perovskite-based materials with PL properties. We investigate the role of microwave processing on the structural and photoluminescent behavior of CT powders. The main objective is to investigate the impact of structural order–disorder on the PL emission associated to octahedral tilting.

This research involves four critical steps:

- (1) synthesis of powders;
- (2) structural disorder characterization to elucidate their relationship with the parent ordered samples;
- (3) establishing the formation mechanisms of the disorder; and more importantly,
- (4) revealing the relationships between structural disorder and the PL property. The purpose is to join both the experimental and theoretical results to explain the different responses of PL emission at room temperature by using a structural disorder motif. To this end, we have used different experimental techniques and first-principle calculations based on the density functional theory (DFT) to carry out a comprehensive investigation of the corresponding structures and electronic properties.

3.3 SAMPLE PREPARATION

Perovskite-based materials can be synthesized by a plethora of preparation methods. Mao et al describe a number of advances that have been made in the synthesis of various ABO₃-type oxides. The most popular techniques include the traditional solid state reaction method, formation through a soft solution chemistry methodology such as a co-precipitation method [27], a hydrothermal method, a solvothermal method [30], alkoxide hydrolysis [31], metal–organic processing [32] and Pechini.

Hydrothermal media provide an effective reaction environment for the synthesis of numerous ceramic materials because of the combined effects of solvent, temperature, and pressure on ionic reaction equilibrium. The conventional hydrothermal (CH) method has become an effective synthetic route for the materials science by dramatically increasing control of the micro/nanometric morphology and orientation.

In addition, this method is environmentally friendly and depends on the solubility of the chemical salts in water under temperature and pressure conditions. The key factors in this method are the vapor pressure and solubility of the chemical salts in water.

In contrast to the CH method which requires a long time (typically half to several days) and high electric power (over a thousand watts), microwave-assisted heating is a greener approach to synthesize materials in a shorter time (several minutes to hours) and with lower energy consumption (hundreds of watts). Consequently, the microwaveassisted route is a rapidly developing area of research which has been demonstrated to be efficient in the processing of many oxides.

Recently, the impact of microwave frequency on the hydrothermal synthesis of nanocrystalline tetragonal BaTiO₃ has been analyzed by Suib et al, indicating that the HTMW process can be a potential and breakthrough way for the synthesis of crystalline CT powders at low temperatures and high heating rates.

The condition of Ca/Ti = 1 corresponds to the composition of the desired CaTiO₃ product which was synthesized using TiCl₄ (99.99%, Aldrich), CaCl₂ · 2H₂O (99.9%, Merck) and KOH (99%, Merck).

Three solutions were prepared: in the first solution 0.05 mol of the TiCl_4 was slowly added to 125 ml of de-ionized water at approximately 0°C under vigorous stirring, forming $\text{TiO}(\text{OH})_2^{++} \text{Cl}^-$. Similarly, 0.05 mol of $\text{CaCl}_2 \cdot 2\text{H}_2\text{O}$ was dissolved in the de-ionized water. Then, two precursor solutions containing Ti^{4+} and Ca^{2+} ions were mixed, homogenized and shared in five portions of 50 ml, to which 50 ml of the KOH solution (6 M) was added to act as a mineralizer [35] and bring to $\text{pH} = 14$.

The suspension was loaded into a 110 ml Polytetrafluoroethene autoclave reaching 90% of its volume, providing the maximum pressure efficiency to the system. The autoclave was sealed and placed into a microwave-assisted hydrothermal system using 2.45 GHz microwave radiation (Support information S1) with a maximum output power of 800 W [44]. The reaction mixture was heated to 140°C in less than 1 min (at 800 W) by a direct interaction of water with microwave radiation and was kept at this temperature for 10 (CT10), 20 (CT20), 40 (CT40), 80 (CT80) and 160 (CT160) min under pressure of 2.5 bar. Afterward the autoclave was naturally cooled to room temperature.

Then the solid product was washed with de-ionized water until a neutral pH was reached and then dried at 80°C for 12 h. The CaTiO_3 reference sample (CTref) was prepared by the polymeric precursor method and heat-treated at 700°C for 2 h in a conventional furnace under an air atmosphere and then naturally cooled to room temperature. This sample did not present photoluminescence properties, and therefore the sample was used as a reference sample (CTref).

3.4 CHARACTERIZATION TECHNIQUES

Structural techniques were employed to provide information on different time and length scales. Each level has its particular complexity, and the results therefore offer structural insight into those length scales that determine many important aspects of material phenomenology and their properties. Also, it is becoming increasingly clear that a detailed microscopic structural understanding of materials is necessary. Thus it is mandatory to use different techniques such as

X-ray diffraction, which enables an average depiction of the structure (through pattern matching and Rietveld analysis).

Moreover, there is a wide range of experimental techniques that can be considered as complementary tools to characterize specific properties of the materials. Both Raman and UV spectroscopies are among the advanced nondestructive characterization tools used to acquire information on the estimate of the structural order at short and medium ranges of a material. Therefore, they can be used to estimate the crystal potential fluctuations and local atomic arrangement. In addition, currently it is well recognized that optical properties like PL depend on both structural and electronic properties, including compositional ordering and the presence of impurities and defects. PL depends on electronic excitations and thus is a necessary complement to spectroscopies concerning lattice excitations, yielding structural information of a completely different character from the information obtained by diffraction- based techniques. The latter detected long-range order while the former yielded information on the immediate surroundings of an ion (particularly useful as a structural probe in short-range amorphous structures).

X-ray absorption near-edge structure (XANES) spectroscopy provides information about the local order around cations in oxide materials. Ti K-edge XANES experimental results of photoluminescent titanates revealed the coexistence of two types of environment of titanium atoms, namely fivefold coordinated TiO_5 (square-base pyramid) and sixfold coordinated TiO_6 (octahedron), before reaching the complete structural order. Based on the Ca Kedge L3,2 XANES spectra, Asokan et al reported changes in the local order around Ca atoms.

Powder X-ray diffraction (XRD) experiments were carried out on the as-prepared samples, and the corresponding measurements were obtained by Rigaku DMax 2500PC using $\text{Cu K}\alpha_1$ ($k = 1.5406 \text{ \AA}^\circ$) and $\text{Cu K}\alpha_2$ ($k = 1.54434 \text{ \AA}^\circ$) radiation. Data were collected from 20° to 120° in 2θ range with an 0.5° divergence slit and an 0.3 mm receiving slit using a fixed-time mode with a 0.02° step size and 1s/point .

The Rietveld refinements were carried out with GSAS software, which is specially designed to simultaneously refine both structural and microstructural parameters using the least-square method. The peak profile function was modeled using the convolution of the Thompson–Cox–

Hastings pseudo-Voigt (pV-TCH) with the asymmetry function described by Finger et al. The background of each pattern was fitted by a polynomial function. Raman spectra were recorded on a RFS/100/S Bruker Fourier transform Raman (FT-Raman) spectrometer with a Nd:YAG laser providing an excitation light at 1064 nm in a spectral resolution of 4 cm^{-1} . An inductively coupled plasma atomic emission spectrometer, ICP-AES Simultaneous CCD–VISTA–MPX (Varian), with radial configuration, was used for chemical analysis. The dissolution procedure was carried out using 10 ml of HCl (37% purity) and 3 ml of HNO₃ (68% m/m) in closed vessels for 2 h at room temperature. Analytical blanks were prepared following the same acid digestion procedure.

Background signal correction was carried out by the operating software of the instruments. The generator frequency was 40 MHz, with an RF power of 100 kW and a plasma gas flow rate of 15 l min⁻¹. Emission bands at 396.8 and 366.1 nm were used to quantify calcium and titanium content, respectively. Microstructural characterization was performed by field emission scanning electron microscopy (FE-SEM, Zeiss SupraTM 35).

Titanium and calcium K-edge X-ray absorption spectra were collected at the LNLS (National Synchrotron Light Laboratory) facility using the D04B-XAS1 beam line. The LNLS storage ring was operated at 1.36 GeV and 160 mA. XANES spectra of grounded samples were collected at the Ti K-edge (4966 eV) and Ca K-edge (4205 eV) in the transmission mode at room temperature using a Si(1 1 1) channel-cut monochromator. XANES spectra were recorded between 4910 and 5100 eV for Ti and 4000 and 4200 eV for the Ca K-edge using energy steps of 0.3 eV. For comparison purposes of the different samples, all spectra were background removed and normalized using as unity the first EXAFS (extended X-ray absorption fine structure) oscillation.

UV–visible absorption was recorded using the Cary 5G spectrometer in total reflection mode by the integration sphere. Photoluminescence (PL) spectra were collected with a Thermal Jarrel-Ash Monospec 27 monochromator and a Hamamatsu R446 photomultiplier. The 350.7 nm exciting wavelength of a krypton ion laser (Coherent Innova) was used, with the nominal output power of the laser kept at 200mW. All measurements were taken at room temperature.

Table 1
Internal and lattice parameters used for theoretical calculations.

	CT _{ref}	CT10	CT160
<i>Lattice parameters</i>			
<i>a</i> (Å)	5.387	5.406	5.405
<i>b</i> (Å)	5.439	5.492	5.489
<i>c</i> (Å)	7.646	7.664	7.662
<i>Internal parameters</i>			
Ti	0000, 0500, 0000	0000, 0500, 0000	0000, 0500, 0000
Ca	0992, 0033, 0250	0989, 0044, 0250	0991, 0043, 0250
O ₁	0072, 0489, 0250	0085, 0484, 0250	0086, 0479, 0250
O ₂	0717, 0284, 0034	0706, 0292, 0037	0708, 0290, 0036

CT_{ref} = reference sample, prepared by the polymeric precursor method.

3.5 COMPUTATIONAL METHOD AND PERIODIC MODEL

The simulation was performed using a periodic approximation as implemented in the CRYSTAL06 computer code. Our computational method is the density functional theory in conjunction with Becke's three parameter hybrid nonlocal exchange functional [55], combined with the Lee–Yang–Parr gradient-corrected correlation functional, B3LYP, which has proven to be a very effective tool to deal with the present challenging problem. We have been particularly successful in employing this functional to study the electronic and structural properties of bulk and surfaces of PbTiO₃, AZrO₃ and several other oxides.

The atomic centers are described by all electron basis sets 86-511(d21)G for Ca, 86-411(d31)G for Ti and 6-31G* for O (Support information S2). The XcrysDen program was used for the band structure drawing design.

The analysis of the vibrational modes and their corresponding frequencies were calculated through numerical second derivatives of the total energies as implemented in the CRYSTAL06 package. Lattice constants and internal coordinate data were obtained from XRD pattern refinement using the Rietveld method to better describe the structural distortion derived from the experimental data.

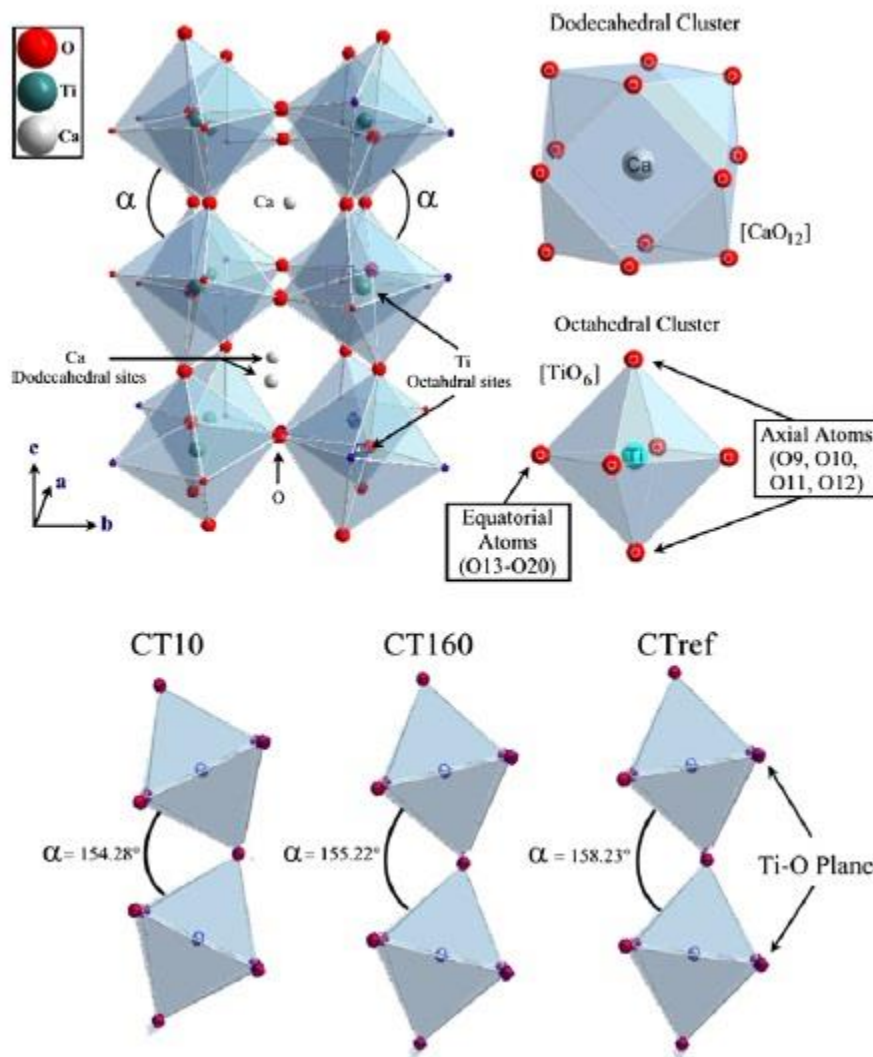


Figure 3.5.1: Different values of α angles for $(\angle O-Ti-O)$ adjacent $[TiO_6]-[TiO_6]$ clusters and a schematic model for CTHTMW with octahedral and dodecahedral sites for Ca and Ti atoms, respectively.

CT crystallizes in an orthorhombic perovskite structure Pbnm space group, in a single phase with four nonequivalent atoms per unit cell, with lattice parameters and internal coordinations obtained from refined parameters.

Internal coordinates and net parameters for CTref, CT10 and CT160 samples are listed in Table 1. The alpha (α) angle values for adjacent TiO₆ octahedra are schematically illustrated in Fig. 3.5.1 together with their octahedral and dodecahedral sites built on the lattice parameters obtained from Rietveld refinements.

Table 2
Nominal and experimental compositions of CT_{HTMW} samples.

Ceramic denomination	Composition in molar fraction	
	Nominal Ca/Ti	Analyzed ^a Ca/Ti
CT10	1	1.062 (± 0.006)
CT20	1	1.065 (± 0.002)
CT40	1	1.055 (± 0.003)
CT80	1	1.037 (± 0.001)
CT160	1	1.023 (± 0.003)

^a $\alpha n = 5(\alpha = \text{analyzed}, n = \text{measures})$.

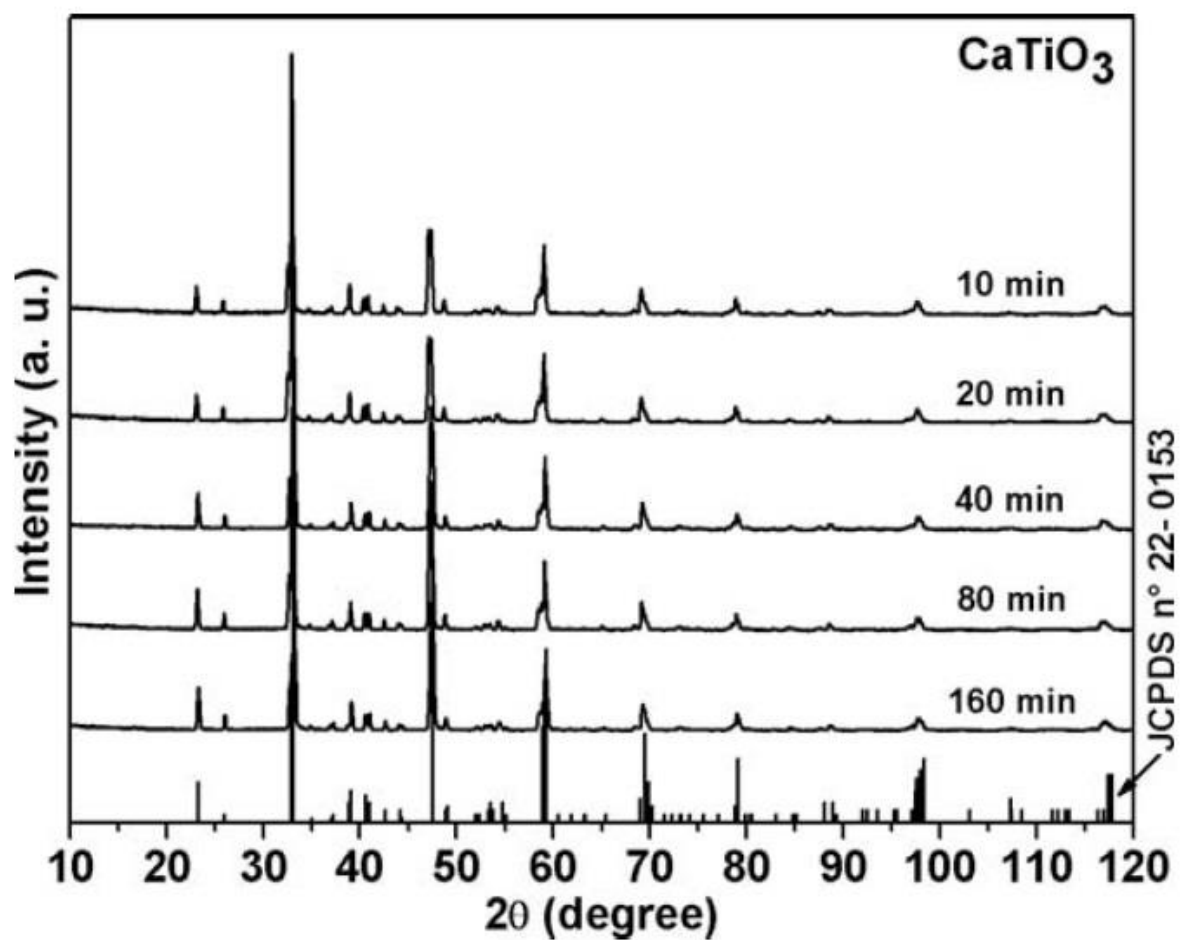


Figure 3.5.2: X-ray patterns of CT samples annealed at 140°C from 10 to 160 min.